Self-Powered Flexible Sensor Array for Dynamic Pressure Monitoring

Li Wu, Jiangtao Xue, Jianping Meng, Bojing Shi, Wei Sun, Engui Wang, Mengji Dong, Xuemei Zheng, Yuxiang Wu, Yusheng Li,* and Zhou Li**

Flexible pressure sensors are valuable in applications such as electronic skin, smart robots, artificial prosthetics, and wearable electronics. In this study, a fully packaged, flexible, self-powered, long-term stable sensor array based on piezoelectrets is developed for pressure monitoring. A pressure sensor with a microcavity structure and a thickness of 500 µm achieved an impressive piezoelectric coefficient of 23.8 pC N^{-1} and a fast response time of 93 ms. The sensor yielded an output voltage of 0.26 V when subjected to a force using 0.3 g soybeans, and it displayed a remarkable linear relationship (R^2 = 0.992) between force and electricity with pressure ranging from 1.4 to 13.6 N and a sensitivity of 9 mV N^{-1}. Real-time monitoring of sound vibration, radial artery pulse, and finger movement is demonstrated along with the successful recording of dynamic pressure changes within the porcine knee joint. It holds potential for fields such as monitoring pressure changes in the movement of human bodies and robotics and can contribute significantly to pressure assessment during total knee replacement.

1. Introduction

Sensor networks have become popular in recent years with the foreseeable advancement in the Internet of Things (IoT) and artificial intelligence (AI). Sensors play key roles in signal conversion and information collection. Pressure sensors are an important branch of sensor networks that have been significantly augmented recently owing to their potential applications in electronic skins,[1] smart robots,[2] artificial prosthetics,[3] and wearable electronics.[4] High-performance pressure sensors, which have high sensitivity, flexibility, fast response, stability, and low power consumption, must be developed to satisfy the demand for progress in IoT and AI.

Today, pressure sensors based on different mechanisms, including the piezoresistive effect,[5–7] capacitive effect,[8–10] triboelectric effect,[11] piezoelectric effect,[12–17] piezoelectret effect,[18–20] have been proven to exhibit the characteristics of low power consumption, excellent stability, and good skin compatibility. The external power consumption of a pressure sensor, which is based on the piezoresistive effect and capacitor changes, renders the device complex.[21–23] Recently, self-powered technologies have provided effective methods to overcome this problem.[24–31] Piezoelectric

L. Wu, Y. Wu
Institute of Intelligent Sport and Proactive Health,Department of Health and Physical Education
Jianghan University
Wuhan 430056, China
E-mail: yxwu@jhun.edu.cn

L. Wu, J. Xue, J. Meng, W. Sun, E. Wang, M. Dong, X. Zheng, Y. Wu, Z. Li
Beijing Institute of Nanoenergy and Nanosystems
Chinese Academy of Sciences
Beijing 101400, China
E-mail: zli@binn.cas.cn

L. Wu, J. Meng, W. Sun, M. Dong, Z. Li
School of Nanoscience and Engineering
University of Chinese Academy of Sciences
Beijing 100049, China

J. Xue
School of Medical Technology
School of Life Science
Beijing Institute of Technology
Beijing 100081, China

B. Shi
Key Laboratory for Biomechanics and Mechanobiology of Ministry of Education, Beijing Advanced Innovation Center for Biomedical Engineering
School of Biological Science and Medical Engineering
Beihang University
Beijing 100191, China

X. Zheng, Z. Li
College of Chemistry and Chemical Engineering
Center on Nanoenergy Research
Guangxi University
Nanning 530004, China

Y. Wu
College of Sports Medicine
Wuhan Sports University
Wuhan 430079, China

Y. Li
Department of Orthopedics, Xiangya Hospital
Central South University
Changsha 410008, China
E-mail: liyusheng@csu.edu.cn

The ORCID identification number(s) for the author(s) of this article can be found under https://doi.org/10.1002/adfm.202316712

DOI: 10.1002/adfm.202316712

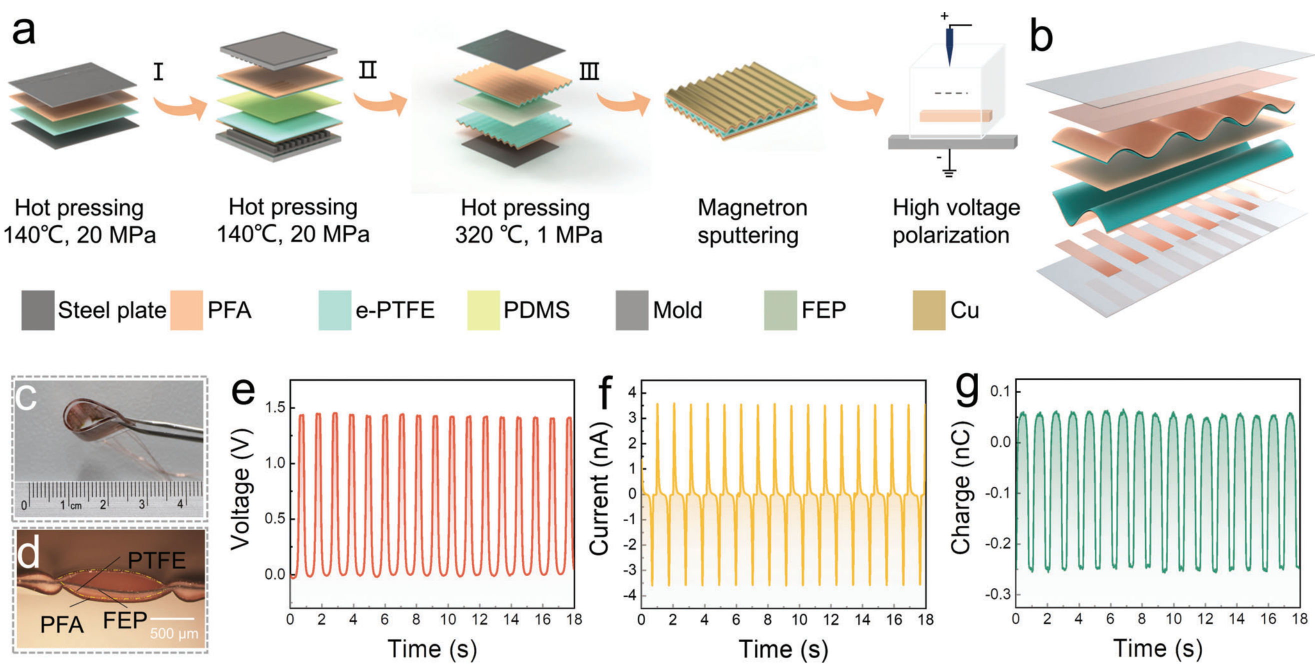

Figure 1. Fabrication process and optical characterization of the pressure sensor. a) Fabrication flow chart of the pressure sensor. b) Structural diagram of the pressure sensor. c) Dimensions of the pressure sensor. d) Microcavity structure of the pressure sensor. e) Output characterization of sensor voltage at a frequency of 1 Hz. f) Output characterization of sensor current at a frequency of 1 Hz. g) Output characterization of the sensor charge at a frequency of 1 Hz.

sensors can achieve sensitive self-powered pressure monitoring through the use of piezoelectric materials with high piezoelectric coefficients.[32–37] Inorganic materials with high piezoelectric coefficients and Young's moduli exhibit high sensitivity; however, their high fragility hinders the flexibility of the device.[38–40] Organic piezoelectric materials such as polyvinylidene fluoride (PVDF) can satisfy the requirements of flexibility, whereas a low piezoelectric coefficient makes it difficult to achieve highly sensitive detection.[41] Organic piezoelectrets with high quasistatic piezoelectric coefficients exhibit comprehensive flexibility and high sensitivity.[42–44] They are widely used to record physiological and acoustic vibration intensity signals in humans.[45–48]

In this study, a fully encapsulated, flexible, self-powered, high-sensitivity, and long-term stable pressure sensor with low cost was prepared to monitor pressure changes in human-body movement using a piezoelectric sensor. This pressure sensor demonstrates highly sensitive detection within the range of 1.4 to 13.6 N. Its rapid response of 93 ms ensures real-time monitoring capabilities for pressure changes. It exhibits impressive resistance to serial interference, with an interelectrode spacing of 1.5 mm. Remarkably, even after 6 months of usage, the piezoelectric coefficient remains constant at 23.8 pC N^{-1}. Additionally, its versatility is evident because it can directly conform to surfaces with varying curvatures. We extend its applicability by affixing a flexible pressure sensor to different body regions. The pressure sensor can monitor the pulse, finger flexion, and sound. Moreover, it has significant potential for monitoring joint flexion and extension movements in pigs. By incorporating a Bluetooth module, the pressure signals can be recorded and visualized on mobile devices. Our approach provides an effective method for surgeons to monitor changes in pressure during joint replacement, which is a comforting task for both patients and surgeons.

2. Results and Discussion

A pressure sensor with a microcavity structure was fabricated using the hot-pressing method. The preparation and characterization of the pressure sensors are shown in **Figure 1**. The pressure sensor was prepared in three steps (Figure 1a). Initially, a stacked composite polymer was formed using the hot-pressing method, which combined expanded polytetrafluoroethylene (e-PTFE) and perfluoroalkoxy (PFA). The presence of porous e-PTFE, which is well known for its excellent charge storage capabilities, significantly enhanced the piezoelectric coefficient.[49,50] PFA, which has superior electrical insulation properties, obstructs the porous structure of e-PTFE, effectively preventing charge neutralization in the surrounding environment. Subsequently, the composite polymer was hot pressed with two patterned metal templates to create a striped structure on the e-PTFE/PFA composite. As a protective measure, a 500 μm thick layer of polydimethylsiloxane (PDMS) is placed between the two sheets of the composite polymer, serving as a buffer layer. This arrangement ensured the added stability of the pressure sensor, contributing to its enhanced functionality and sensitivity. The patterned e-PTFE/PFA composite polymers were cross-placed, forming a specific configuration. To separate the two layers effectively, we inserted fluorinated ethylene propylene (FEP) films with a thickness of 25 μm between them. For the subsequent hot pressing, a lower pressure and higher temperature were employed to preserve the microstructure and facilitate its formation of the microcavity

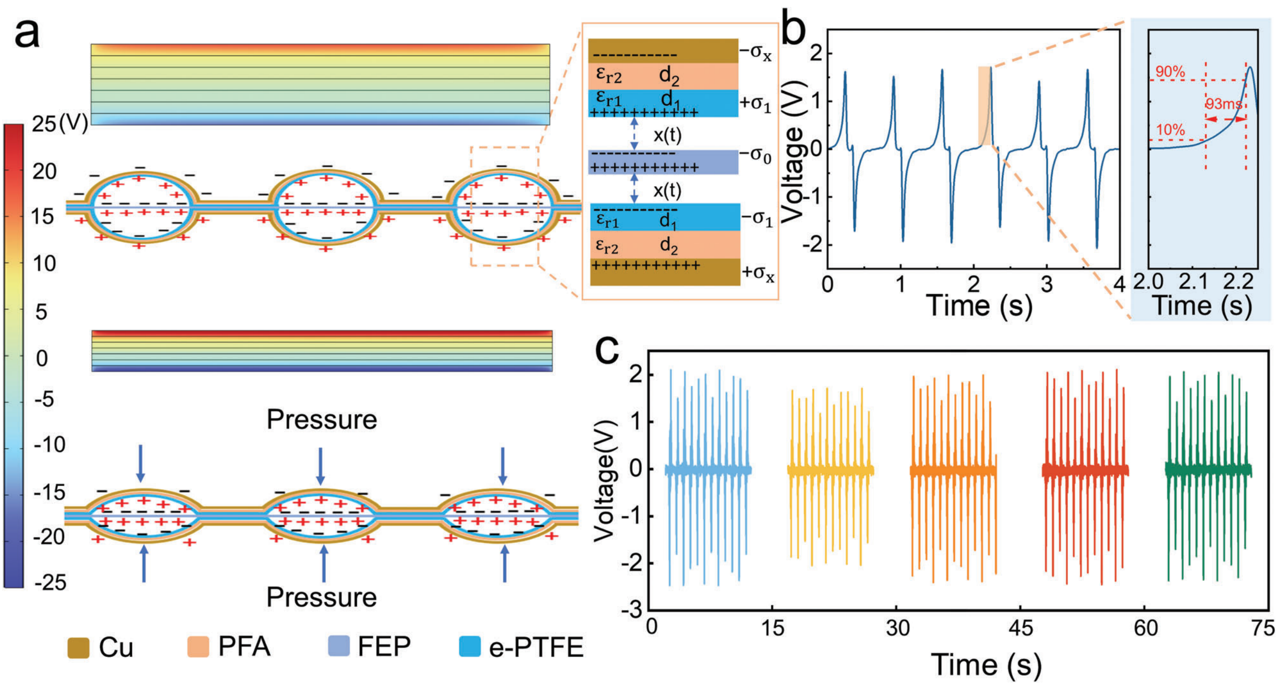

Figure 2. a) Potential distribution in the original state and pressed state of the sensor simulated using finite element simulation. b) Response time of the sensor. c) Output of different channels under the same contact area and force.

structure. This innovative approach results in the creation of a flexible composite electret material with a multi-cavity structure. Microcavities, similar to lens-like structures, play a dual role in enhancing the pressure performance of the sensors. The inclusion of microcavities not only reduces the Young's modulus of the thin film, making the sensor more pliable, but also significantly enhances its piezoelectric capabilities.[51] Next, Cu electrodes were coated onto the surface of the composite material via DC sputtering. Finally, polarization with a corona needle at a high voltage was implemented to generate a lingering charge on the e-PTFE surface. This final step ensured that the electret characteristics of the pressure sensor, which were critical for its functioning, were established. Figure 1b shows the detailed layered structure of the pressure sensor and provides a clear visual representation of its innovative design and components. As shown in Figure 1c, the pressure sensor is flexible, enabling it to bend at various angles with ease. The cross-sectional optical image in Figure 1d provides a clear visualization of the microcavity structure sandwiched between the e-PTFE/PFA and FEP layers. The thickness of the pressure sensor was set as 500 µm. The two surfaces of the pressure sensor displayed striped Cu electrodes as well as the entire Cu electrode. The microcavity, resulting from the combination of low Young's modulus e-PTFE and PFA, acted as an effective charge storage unit, contributing to the exceptional flexibility and high piezoelectric coefficient of the sensor.[49,52] In a performance comparison between PFA/e-PTFE and FEP/e-PTFE (Figure S1, Supporting Information), the pressure sensor prepared with PFA/e-PTFE exhibited superior performance under the same force per unit area. Furthermore, a performance comparison under different contact areas demonstrated a correlation with the contact area. For instance, under a consistent force, the contact area of 0.75 cm^2 (1.5×0.5 cm^2) achieved an output voltage of 5.05 V when using a contact object with a cuboid (Figure S2, Supporting Information). In contrast, the output voltage decreased to 1.14 V when employing a hemisphere with a radius of 0.5 cm as the contact object. The output performances of the individual arrays were investigated, including the voltage, current, and charge, with a force of 1.3 N applied at a frequency of 1 Hz and a contact area of 0.75 cm^2. The recorded output values were a voltage of 1.4 V, a current of 3.5 nA, and a charge of 0.25 nC (Figure 1e–g). The slight differences observed in each pulse (voltage, current, and charge) indicated the stability of the pressure sensors.

During the polarization process, intermittent plasma was generated in the air around the needle electrodes and the air inside the lens-like cavity, and the ions and electrons were trapped by the surfaces of the e-PTFE and FEP. To gain further insight into the potential distribution and charge transfer in the pressure sensor, we conducted a finite element simulation analysis using the software COMSOL (**Figure** 2a). In the original state, the dipoles inside a high-voltage polarized electret create an internal potential, resulting in the accumulation of positive and negative charges at the top and bottom of the electret, respectively. This charge accumulation establishes a potential difference. According to the theoretical electret model shown in Figure 2a, the relationship of the air gap distance x(t) with the electret charge transfer quantity Q_{SC} and open-circuit voltage V_{OC}, as well as the output voltage V and air gap distance x(t) expression functions, can be deduced when the device is operating.

First, the voltage difference of ΔV_E between the upper and lower electrodes can be obtained using Equation (1) in the Supporting Information according to Gauss's theorem of the electromagnetic field.[53] If $\Delta V_E = 0$, we can obtain the relationship

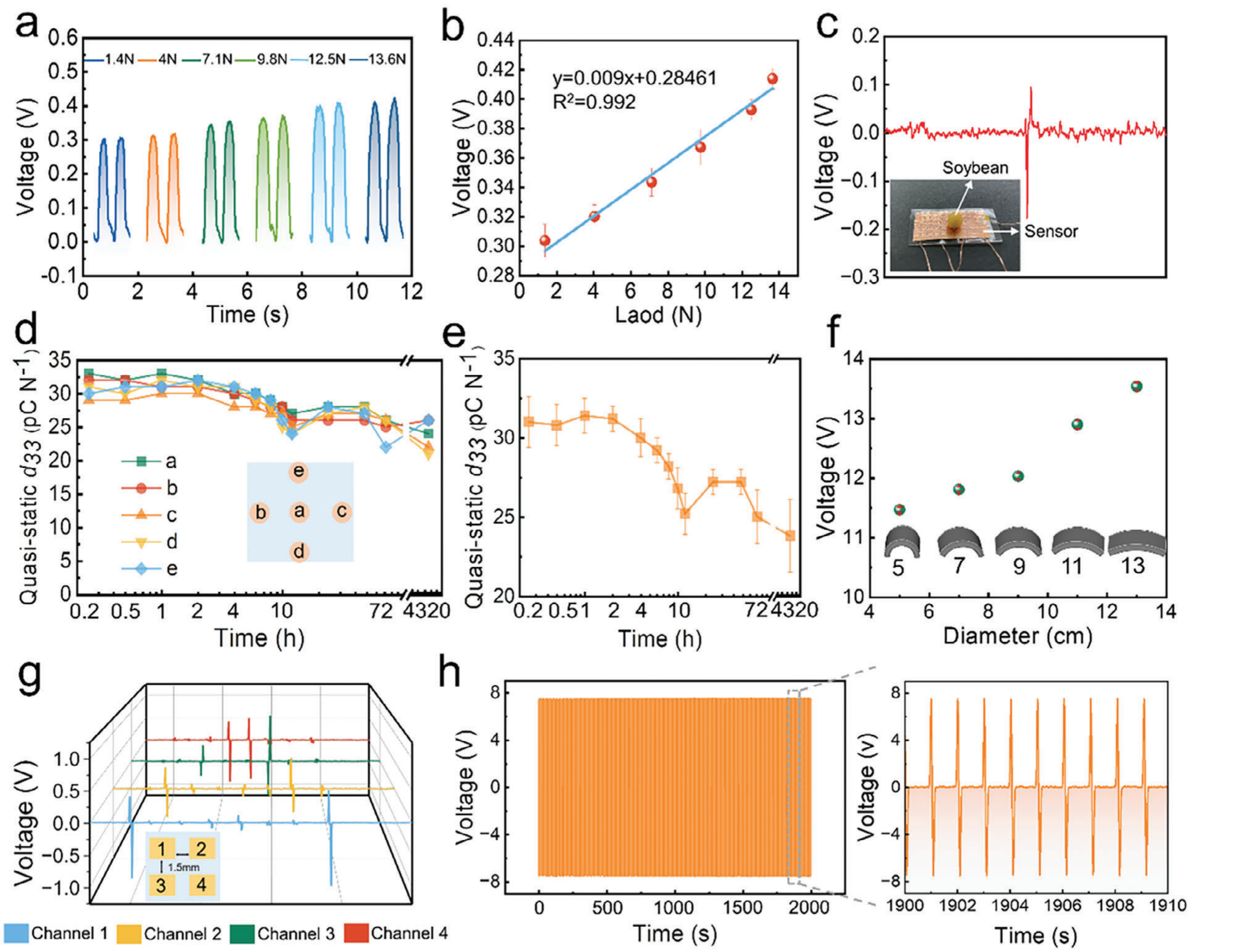

Figure 3. Performance characterization of the flexible pressure sensor. a) Voltage output of the sensor under different loads. b) Relationship between pressure and voltage of the sensor under different loads. c) Minimum detection limit of a flexible pressure sensor. d) Piezoelectric coefficients at different positions of the sensor. e) Average value of sensor piezoelectric coefficient at different times. f) Under the action of an arch structure with different curvatures, the output of the flexible pressure sensor changes. g) Ability of the flexible pressure sensor to resist serial interference. h) Change in voltage output of flexible pressure sensor under 4000 times of action. Data presented as mean ± S.E.M.

between surface charge density σ_x generated by electret electrostatic induction and air gap x(t) according to Equation (2) in Supporting Information.

Therefore, the charge transfer quantity Q_{SC} produced by the triboelectric effect can be expressed as

$$Q_{SC} = \sigma_x \cdot S = \frac{(\sigma_1 - \sigma_0)\, S \frac{d_0}{\varepsilon_{r0}} + \sigma_1 S \cdot 2x(t)}{d_e + 2x(t)} \tag{1}$$

where σ_x is the surface charge density induced by the upper and lower electrodes, σ_0 and σ_1 are the surface charge densities polarized by FEP and e-PTFE after high voltage polarization, respectively. ϵ_{r0} is the dielectric constant of FEP. The effective thickness constant is defined as the sum of the ratios of the thickness of all dielectric materials between the two electrodes and their relative permittivity: $d_e = \frac{d_0}{\varepsilon_{r0}} + \frac{2d_1}{\varepsilon_{r1}} + \frac{2d_2}{\varepsilon_{r2}}$.[54] For the open circuit between the upper and lower conductive layers ($\sigma_x = 0$), V_{OC} of the device can be obtained using

$$V_{OC} = \frac{(\sigma_1 - \sigma_0)}{\varepsilon_0} \frac{d_0}{\varepsilon_{r0}} + \frac{\sigma_1}{\varepsilon_0} \cdot 2x(t) \tag{2}$$

From Equations (1) and (2), the standard form of the V-Q-x relation of the electret can be given by

$$V = \frac{-Q}{S\varepsilon_0}\left(d_e + 2x(t)\right) + \frac{(\sigma_1 - \sigma_0)}{\varepsilon_0} \frac{d_0}{\varepsilon_{r0}} + \frac{\sigma_1}{\varepsilon_0} \cdot 2x(t) \tag{3}$$

where ϵ_0 is the vacuum permittivity, and d_0 is the thickness of the FEP. The charge quantity Q accumulated by the conductive metal layer is equal to the product of the charge density σ_x of the conductive layer and the area S of the conductive layer.

We characterized the performance of the flexible pressure sensor by analyzing its voltage amplitude, as shown in **Figure 3**. The mechanical–electrical relationship, which is determined by

Table 1. Summary of the reported pressure sensors and their performances.

Mechanisms	Materials	Sensitivity	Limit of detection	Response time	Self-powered	Refs.
Piezo resistance	GO/paper	0.02 kPa^{-1}	300 Pa	120 ms	×	[5]
Piezo resistance	PTNWs/G	9.4×10^{-3} μA kPa^{-1}	0.04 N	5–7 ms	×	[6]
Piezo resistance	SEBS/Ag Nanoparticles	71.07 kPa^{-1}	/	<2 ms	×	[7]
		7.38 kPa^{-1}				
		0.01 kPa^{-1}				
Capacitance	PDMS/PPy/GF	2.01 kPa^{-1}	18 Pa	20 ms	×	[8]
Capacitance	PVDF/PDMS	0.43 kPa^{-1}	4 Pa	33 ms	×	[9]
Capacitance	BNF@PDMS	0.29 kPa^{-1}	0.5 KPa	/	×	[10]
		0.854 kPa^{-1}				
Triboelectricity	PDMS/EVA/PET	0.06 kPa^{-1}	1 kPa	70 ms	√	[11]
Piezoelectricity	PVDF/Mxene	41.3 nA kPa^{-1}	2 KPa	41 ms	√	[12]
Piezoelectricity	PVDF/FDTS	134.3 mV N^{-1}	/	/	√	[13]
Piezoelectricity	PVDF/MOFs	0.118 V/N	/	/	√	[14]
Piezoelectricity	P(VDF-TrFE)/BT	2.615 mV kPa^{-1}	7 KPa	/	√	[15]
Piezoelectricity	PVDF/ZnO	3.12 mV kPa^{-1}	/	55 ms	√	[16]
Piezoelectricity	$BaTiO_3$	5.4 mV kPa^{-1}	/	80 ms	√	[17]
Ferroelectret	P(VDF-HFP)/PtNPs	686 pC N^{-1}	/	3 ms	√	[18]
Piezoelectret	Porous PTFE/PTFE	1.5 V kPa^{-1}	/	/	√	[19]
Piezoelectret	FEP/Ecoflex/FEP	32.6 nA kPa^{-1}	125 Pa	/	√	[20]
		6.71 nA kPa^{-1}				
Piezoelectret	PFA/e-PTFE/FEP	9 mV N^{-1}	0.03 N	93 ms	√	This work

measuring its electrical response to applied force, is crucial to the performance of the pressure sensor, and it demonstrated a strong linear relationship between pressure and electrical parameters within the range of 1.4–13.6 N (Figure 3a,b). A 0.5 cm radius hemisphere was employed as a contact object to evaluate the mechanical–electrical relationship of the sensor. Further details regarding the output characterization of the current and charge are shown in Figures S3 and S4 (Supporting Information). To quantify the sensitivity of the sensor, we define sensitivity S as the change in output voltage over a given pressure range ($S = \Delta V/\Delta P$), where V represents the sensor's output voltage and P is the applied pressure. The sensitivity of the pressure sensor was 9 mV N^{-1} (Figure 3b), and the response time was only 93 ms (Figure 2b). We evaluated the lowest detection limit of the pressure sensor using 0.3 g soybeans, resulting in a voltage output of 0.26 V (Figure 3c). We also measured the quasi-static d_{33} values at different locations on the device, and we observed that the value gradually stabilized to 23.8 pC N^{-1} after half a year (Figure 3d,e). Moreover, the performance of the sensor under the influence of varying arch structures with different curvatures was analyzed, revealing an increase in the voltage output with an increase in curvature (Figure 3f). The anti-serial interference ability is another significant characteristic of our sensor, as demonstrated by sputtering array electrodes with a spacing of 1.5 mm on the sensor surface and subjecting them to pressing tests (Figure 3g). Additionally, the sensor exhibited remarkable fatigue resistance, maintaining a stable voltage output even after 4000 cycles of pressing on a linear motor (Figure 3h). To verify the uniformity of our sensor, we conducted tests on five channels of the sensor on the same contact surface under identical forces. The output results exhibited noticeable consistency (Figure 2c). **Table 1** compares the proposed pressure sensors based on various mechanisms, including piezoresistive, capacitive, piezoelectric, triboelectric, and piezoelectric electret mechanisms. The pressure sensor in our study exhibited superior sensitivity, response time detection limit, anti-serial interference resistance, and fatigue resistance.

Flexible pressure sensors can be attached to human skin and joints to convert weak mechanical deformations into electrical signals for real-time monitoring. These include sound vibrations, pulse rhythms, finger movements, and knee-joint actions (**Figure 4**). For instance, when placed on the larynx, the sensor records voltage output changes corresponding to the production of the "ah" sound (Figure 4a). Employing an elastic bandage, we attached a sensor to a radial artery to monitor pulse beats. As shown in Figure 4b, the sensor directly monitored the vasodilation and contraction states of the cardiac cycle. The adaptability of the sensor extends to finger flexion and extension where muscle contraction occurs at the back of the hand. Figure 4c shows the output voltage used to monitor finger movement when the sensor was placed at the back of a hand. We also monitored the dynamic knee pressure in vitro. The pressure sensor was attached to the tibial component of the prosthetic knee joint (Figure 4d). Electromechanical relationships can be used to obtain real-time dynamic pressure maps during joint flexion and extension. These data can be transmitted via Bluetooth and displayed on a screen

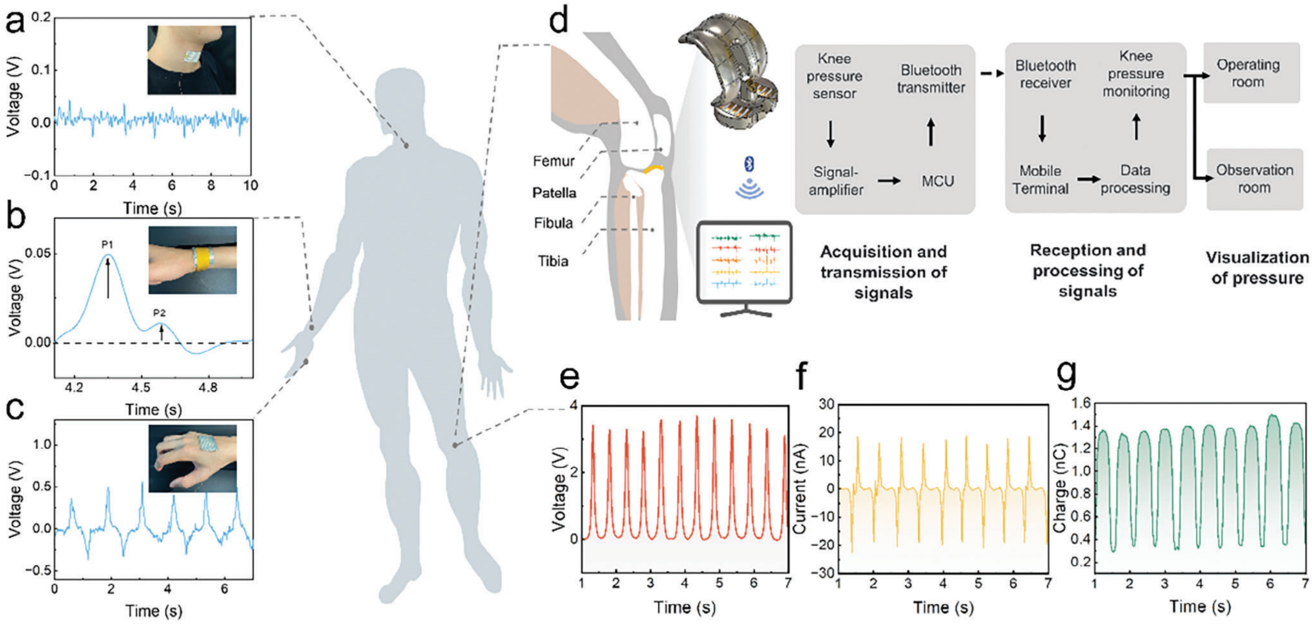

Figure 4. Application of flexible pressure sensor in the human body. a) Monitoring sound vibration. b) Monitoring radial artery pulse. c) Monitoring finger flexion and extension. d) Wireless transmission of knee joint pressure concept map. e) Output characterization of voltage during the rolling process of the sensor on the knee joint mold. f) Output characterization of current during the rolling process of the sensor on the knee joint mold. g) Output characterization of charge during the rolling process of the sensor on the knee joint mold.

(Figure S5 and Video S1, Supporting Information). The knee joint is always flexed and extended along its sagittal axis of the knee joint,[55] and the medial and lateral condyles of the lower end of the femur are always aligned when they are in contact with the sensor. Employing a knee joint mold to simulate real pressure conditions, the sensor consistently yielded stable outputs, including a voltage of 3.5 V, a current of 20 nA, and a charge of 1.4 nC (Figure 4e–g). Subsequently, flexible sensor electrodes were designed as multi-channel arrays (see Experimental Section for details) and placed in a knee prosthesis for dynamic pressure monitoring. Distinctive spike voltage signals emerged as the knee joint transitioned from 0° to 120°, providing clear indications of movement (Figure S6, Supporting Information). These voltage spikes signify real-time alterations in the pressure and knee joint position, effectively capturing the dynamic nature of joint motion. The stability of pressure sensors across individuals plays an important role in their clinical applications. To assess this, we meticulously selected six knee prostheses with sizes ranging from 62 to 80, corresponding to individuals of different heights, for stability measurements. In various types of knee prostheses, the pressure ratio of the third channel between the medial and lateral condyles was stable at ≈1.64 at 60° of flexion (Figure S7 and Table S1, Supporting Information). These results collectively confirmed the stability and universal applicability of the pressure sensors. In total knee replacement, the gap between the knee joint and the articular disc has crucial implications for the postoperative recovery of patients. An unsuitable space results in an unbalanced force on the surface of the knee joint prosthesis and articular disc. Unbalanced force is generally measured in knee arthroplasty. We simulated unbalanced force scenarios on the medial and lateral condyles across angles ranging from 0° to 120°. When the knee was tilted 5° toward the medial or lateral condyle, a significant difference was observed in the five-channel pressure signal obtained by the flexible sensor at each angle (Figures S8 and S9 and Tables S2 and S3, Supporting Information). Overall, these results underscored the capacity of the pressure sensor to instantaneously reflect real-time knee-joint tilting at different angles.

As previously highlighted, our pressure sensor exhibits both flexibility and resistance to serial interference. Moreover, the consistent performance across each channel underscores its suitability for knee-joint pressure analysis. This multi-channel pressure sensor with a thickness of 500 µm can be seamlessly affixed to the tibial prosthesis of the knee joint, enabling the monitoring of pressure variations across different flexion and extension angles. Animal experiments were performed to verify that the flexible sensor functioned properly during total knee replacement (**Figure 5**). We conducted a total knee replacement on the porcine knee joint (Figure 5a) and affixed flexible sensors to the tibial prosthesis. This, in conjunction with the external signal-receiving device, formed a dynamic pressure-monitoring system for the knee joint (Figure 5b). Owing to the size of the pig knee joint, the electrode array of the flexible sensor was reduced to four channels. During pig knee flexion from the initial position to 100°, the pressure changes in the joint at varying angles were recorded in real time by the sensor (Figure 5c; Video S2, Supporting Information). The distance between the voltage spikes at different angles indicated the speed of both flexion and extension. The porcine knee was consistently flexed at an initial angle of 30°.[56] Notably, during flexion and extension, the pressure exerted on the medial condyle of the articular disc outweighed that exerted on the lateral condyle. Upon flexion to 60°, the pressure values of the third channel of the medial and lateral condyles were recorded as 68.4 and 40.6 N (voltage amplitudes of 0.9 and 0.65 V). Consequently, the pressure ratio was 1.68, which aligned with the simulated

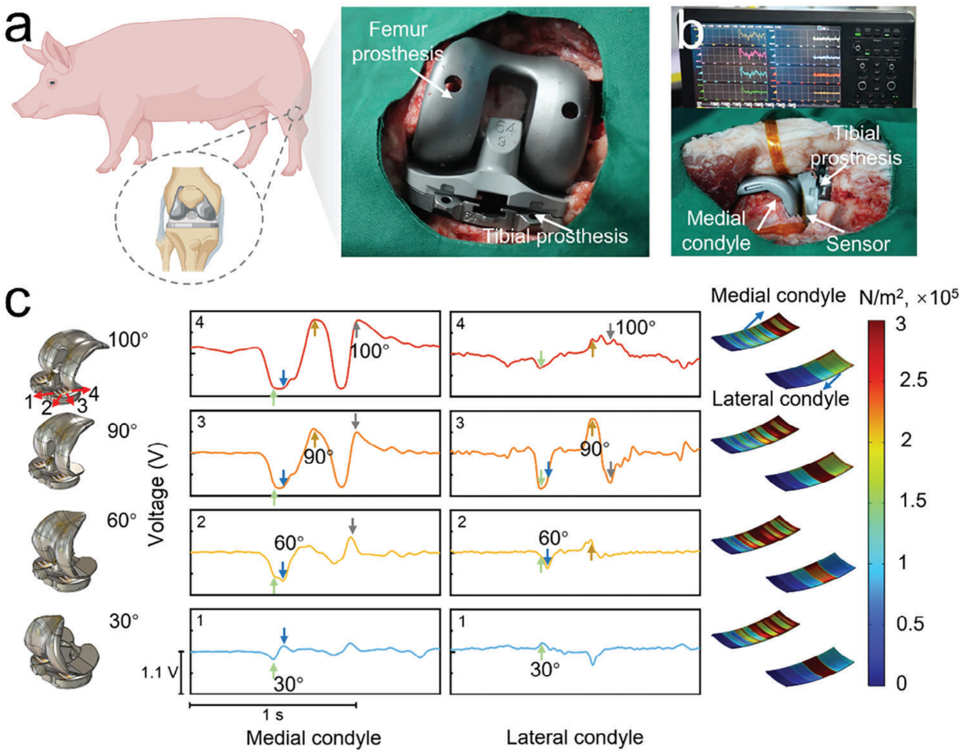

Figure 5. Dynamic pressure monitoring during knee arthroplasty in pigs. a) Schematic representation of pig total knee replacement. b) Dynamic knee pressure monitoring system in animal experiments. c) Force distribution of the knee joint under different joint angles of pigs.

force scenario of the in vitro joint mold (Table S4, Supporting Information). When the medial and lateral condyles were in a state of force imbalance in total knee arthroplasty, the flexible sensors could also monitor this in real time (Figures S10 and S11 and Tables S5 and S6, Supporting Information). This finding is particularly significant in scenarios where this information is used to improve surgical precision by enabling on-the-fly adjustments to the degree of fixation and overall accuracy, such as total knee replacement. Because of its low cost and ease of use, it can be used as a disposable pressure-sensing device replacement. Moreover, it can revolutionize clinical teaching by providing an intuitive and detailed perspective on the surgical process, offering educators and trainees invaluable resources for learning and skill development.

3. Conclusion

We developed and realized a cutting-edge solution: a flexible, fully encapsulated, self-powered, and long-term stable pressure sensor based on piezoelectric electret principles. The 500-µm thick sensor fabricated using the hot-pressing method has a microcavity structure and achieves an impressive piezoelectric coefficient of 23.8 pC N^{-1}, rendering the high sensitivity to the pressure change. This performance was demonstrated by an experiment in which a force of 0.3 g soybeans generated a voltage of 0.26 V. Its swift response time of 93 ms underscores the real-time monitoring capabilities. The output performance and piezoelectric coefficient displayed high stability even after 4000 cycles and 6 months of usage. The pressure sensor shows a remarkable linear relationship ($R^2 = 0.992$) for the mechanical–electrical relationship when the pressure is from 1.4 to 13.6 N, and the sensitivity calculated from the mechanical–electrical relationship is 9 mV N^{-1}, indicating it can detect the pressure change in the low-pressure range. The practicality of this innovation extends its application to human skin and joint surfaces, enabling the dynamic tracking of human body movements. Furthermore, when adhered to a knee joint mold, it can effectively monitor pressure variations and bending angles during flexion and extension of the knee joint. The collected pressure signals were wirelessly transmitted to an external screen for visualization. Therefore, the implications of the pressure sensor are significant. It has potential applications in monitoring pressure changes in the movement of human bodies and robotics. The successful recording of dynamic pressure changes after knee arthroplasty in pigs offered valuable contributions to the assessment of pressure during subsequent total knee replacement. This advancement marks a pivotal step forward in pressure-sensing technology with the capacity to enhance both healthcare practices and technological advancements.

4. Experimental Section

Device Preparation: e-PTFE (30 µm thick) with 60% porosity and PFA (25 µm thick) were cut into a 10 × 10 cm^2 square and put between the stainless steel plates to make a two-layer PFA/e-PTFE composite polymer film. This was done by hot pressing (140 °C, 20 MPa, 3 min). Subsequently, a layer of PDMS with a thickness of 500 µm was placed between the two PFA/e-PTFE composite polymers as a buffer layer and was pressed for 3 min using two stainless steels with a stripe structure under a temperature of 140 °C and a pressure of 20 MPa. Finally, a 25-µm thick FEP layer was pressed between the two PFA/e-PTFE layers to act as a spacer. This was done by hot pressing (1 MPa, 320 °C, 5 min). Flexible piezoelectric composite materials with multi-cavity structures were prepared. The arrayed copper electrode was then deposited through magnetron sputtering using a template. Oriented macrodipoles were generated inside the microcavities after high-voltage polarization using a negative voltage of 5 kV for 15 min. PDMS was used to cover the whole device by spin coating after silver paste was used to connect the wires to the electrodes. This kept the electrons from being neutralized by the charged environment.

Characterization of the Device: The mechanical-electrical relationship was confirmed using a MARK-10 instrument equipped with a force sensor. A quasistatic d_{33} instrument (ZJ-4AN) was used to measure the piezoelectric coefficients of the sensors at different periods. A Keithley 6517 system and a Tektronix oscilloscope (HD06104) were used to collect the electrical signals under pressures ranging from 1.4 to 13.6 N. The force was calibrated and recorded using a Mark-10 instrument. The cavity structure of the device was characterized using optical and scanning electron microscopy. A quasi-static d_{33} measuring instrument (ZJ-4AN) measured the piezoelectric coefficient. Using an oscilloscope and an electrometer, it was possible to assess the stability and long-term performance of the linear motor-driven knee joint. The frequency of the linear motor is 1 Hz.

In Vitro Test: To monitor sound vibration and finger flexion and extension, Kapton double-sided tape fixed the flexible sensor array to the skin's surface. To simulate the dynamic pressure change of the knee joint, a pressure sensor array was fixed on the mold of the knee joint to measure the pressure change at different angles.

Animal Experiment: The leg hairs were removed by using a removal cream, and the knee joint skin was prepared with a tincture of iodine solution. Subsequently, the skin (wound size 20 cm) was incised in the anterior median of the knee, the excess infrapatellar fat was removed, and the joint capsule was cleaned to expose the knee joint. After cutting out the cruciate ligament, meniscus, and extra soft tissue, the knee joint was dislocated and an osteotomy was made using the positioning system and the four-in-one osteotomy plate. The knee prosthesis (BFPSI61H9) was then put in place. The flexible sensor array was attached to the plane of the tibial prosthesis using Kapton double-sided tape to monitor the balance of the medial and lateral spaces. The knee flexion and extension angles were recorded by a Sony camera (A7M3). The experiments involving human subjects were performed with the full, informed consent of the volunteers, who are also authors of the manuscript. All experiments were approved by the Committee on Ethics of the Beijing Institute of Nanoenergy and Nanosystems (2022009LZ).

Statistical Analysis: The mean value and standard error of the mean (S.E.M.) of the data were determined by descriptive statistics. In the test of the mechanical-electrical relationship, three loading cycles of the pressure were performed. In the piezoelectric coefficient attenuation test, the quasi-static d_{33} values were obtained at different times from five points. The sensor response tests for arch structures were repeated with varying curvatures three times. Data were analyzed as mean ± S.E.M. in GraphPad Prism v. 6. Origin 2018, and GraphPad Prism v. 6 were used for data plotting.

Supporting Information

Supporting Information is available from the Wiley Online Library or from the author.

Acknowledgements

L.W., J.X., and J.M. contributed equally to this work. The authors are thankful for the support provided by the National Key R & D Project from Minister of Science and Technology (2022YFB3804703, 2022YFB3804704, and 2023YFB3208101), the National Natural Science Foundation of China (T2125003, 82071970, and 32101117), the Natural Science Foundation of Beijing Municipality(L212010), the Science Fund for Distinguished Young Scholars of Hubei Province (2023AFA109), and the Fundamental Research Funds for the Central Universities.

Conflict of Interest

The authors declare no conflict of interest.

Data Availability Statement

Research data are not shared.

Keywords

flexible, long-term stable, microcavity, piezoelectrets, pressure sensor

Received: December 27, 2023
Revised: February 22, 2024
Published online:

[1] D. Chen, Q. Pei, *Chem. Rev.* **2017**, *117*, 11239.
[2] J. An, P. F. Chen, Z. M. Wang, A. Berbille, H. Pang, Y. Jiang, T. Jiang, Z. L. Wang, *Adv. Mater.* **2021**, *33*, 2101891.
[3] Z. Y. Shi, L. X. Meng, X. L. Shi, H. P. Li, J. Z. Zhang, Q. Q. Sun, X. Y. Liu, J. Z. Chen, S. R. Liu, *Nano-Micro Lett.* **2022**, *14*, 141.
[4] J. Xue, Y. Zou, Y. Deng, Z. Li, *EcoMat* **2022**, *4*, e12209.
[5] L. Q. Tao, K. N. Zhang, H. Tian, Y. Liu, D. Y. Wang, Y. Q. Chen, Y. Yang, T. L. Ren, *ACS Nano* **2017**, *11*, 8790.
[6] Z. F. Chen, Z. Wang, X. M. Li, Y. X. Lin, N. Q. Luo, M. Z. Long, N. Zhao, J. B. Xu, *ACS Nano* **2017**, *11*, 4507.
[7] F. C. Liang, H. J. Ku, C. J. Cho, W. C. Chen, W. Y. Lee, W. C. Chen, S. P. Rwei, R. Borsali, C. C. Kuo, *J. Mater. Chem. C* **2020**, *8*, 5361.
[8] H. Park, J. W. Kim, S. Y. Hong, G. Lee, D. S. Kim, J. H. Oh, S. W. Jin, Y. R. Jeong, S. Y. Oh, J. Y. Yun, J. S. Ha, *Adv. Funct. Mater.* **2018**, *28*, 1707013.
[9] Z. B. Luo, J. Chen, Z. F. Zhu, L. Li, Y. Su, W. Tang, O. M. Omisore, L. Wang, H. Li, *ACS Appl. Mater. Interfaces* **2021**, *13*, 7635.
[10] R. Y. Tay, H. L. Li, J. J. Lin, H. Wang, J. S. K. Lim, S. Chen, W. L. Leong, S. H. Tsang, E. H. T. Teo, *Adv. Funct. Mater.* **2020**, *30*, 1909604.
[11] X. D. Wang, H. L. Zhang, L. Dong, X. Han, W. M. Du, J. Y. Zhai, C. F. Pan, Z. L. Wang, *Adv. Mater.* **2016**, *28*, 2896.
[12] C. Han, H. Zhang, Q. Chen, T. Li, L. J. Kong, H. Zhao, L. R. He, *Chem. Eng. J.* **2022**, *450*, 138280.
[13] H. Li, S. Lim, *J. Mater. Chem. A* **2022**, *10*, 14894.
[14] B. H. Moghadam, M. Hasanzadeh, A. Simchi, *ACS Appl. Nano Mater.* **2020**, *3*, 8742.
[15] N. T. Tien, S. Jeon, D. I. Kim, T. Q. Trung, M. Jang, B. U. Hwang, K. E. Byun, J. Bae, E. Lee, J. B. H. Tok, Z. N. Bao, N. E. Lee, J. J. Park, *Adv. Mater.* **2014**, *26*, 796.
[16] T. Yang, H. Pan, G. Tian, B. B. Zhang, D. Xiong, Y. Y. Gao, C. Yan, X. Chu, N. J. Chen, S. Zhong, L. Zhang, W. L. Deng, W. Q. Yang, *Nano Energy* **2020**, *72*, 104706.
[17] J. H. Yan, Y. H. Han, S. H. Xia, X. Wang, Y. Y. Zhang, J. Y. Yu, B. Ding, *Adv. Funct. Mater.* **2019**, *29*, 1907919.
[18] S. K. Ghosh, T. K. Sinha, B. Mahanty, D. Mandal, *Energy Technol.* **2015**, *3*, 1190.
[19] X. Zhang, X. Zhang, G. M. Sessler, X. Gong, *J. Phys. D: Appl. Phys.* **2014**, *47*, 015501.
[20] Y. Chu, J. Zhong, H. Liu, Y. Ma, N. Liu, Y. Song, J. Liang, Z. Shao, Y. Sun, Y. Dong, X. Wang, L. Lin, *Adv. Funct. Mater.* **2018**, *28*, 1803413.
[21] S. Sharma, A. Chhetry, P. Maharjan, S. Zhang, K. Shrestha, M. Sharifuzzaman, T. Bhatta, Y. Shin, D. Kim, S. Lee, J. Y. Park, *Nano Energy* **2022**, *95*, 106970.
[22] Y. Ke, K. Jia, W. Zhong, X. Ming, H. Jiang, J. Chen, X. Ding, M. Li, Z. Lu, D. Wang, *Chem. Eng. J.* **2022**, *435*, 135003.

[23] K.-H. Ha, H. Huh, Z. Li, N. Lu, *ACS Nano* **2022**, *16*, 3442.
[24] Z. Liu, Y. Ma, H. Ouyang, B. Shi, N. Li, D. Jiang, F. Xie, D. Qu, Y. Zou, Y. Huang, H. Li, C. Zhao, P. Tan, M. Yu, Y. Fan, H. Zhang, Z. L. Wang, Z. Li, *Adv. Funct. Mater.* **2019**, *29*, 1807560.
[25] Z. L. Wang, J. Song, *Science* **2006**, *312*, 242.
[26] F.-R. Fan, Z.-Q. Tian, Z. L. Wang, *Nano Energy* **2012**, *1*, 328.
[27] L. Liu, X. Guo, W. Liu, C. Lee, *Nanomaterials* **2021**, *11*, 2975.
[28] Z. Liu, S. Zhang, Y. M. Jin, H. Ouyang, Y. Zou, X. X. Wang, L. X. Xie, Z. Li, *Semicond. Sci. Technol.* **2017**, *32*, 064004.
[29] Z. Y. Zhang, C. H. Yao, Y. H. Yu, Z. L. Hong, M. J. Zhi, X. D. Wang, *Adv. Funct. Mater.* **2016**, *26*, 6760.
[30] P. K. Yang, L. Lin, F. Yi, X. H. Li, K. C. Pradel, Y. L. Zi, C. I. Wu, J. H. He, Y. Zhang, Z. L. Wang, *Adv. Mater.* **2015**, *27*, 3817.
[31] Y. Wu, Y. Li, Y. Zou, W. Rao, Y. Gai, J. Xue, L. Wu, X. Qu, Y. Liu, G. Xu, L. Xu, Z. Liu, Z. Li, *Nano Energy* **2022**, *92*, 106715.
[32] H. C. Liu, J. W. Zhong, C. Lee, S. W. Lee, L. W. Lin, *Appl. Phys. Rev.* **2018**, *5*, 041306.
[33] P. Tan, Y. Xi, S. Chao, D. Jiang, Z. Liu, Y. Fan, Z. Li, *Biosensors* **2022**, *12*, 234.
[34] L. Lu, W. Ding, J. Liu, B. Yang, *Nano Energy* **2020**, *78*, 105251.
[35] Z. Li, G. A. Zhu, R. S. Yang, A. C. Wang, Z. L. Wang, *Adv. Mater.* **2010**, *22*, 2534.
[36] C. L. Sun, J. Shi, D. J. Bayerl, X. D. Wang, *Energy Environ. Sci.* **2011**, *4*, 4508.
[37] C. M. Boutry, A. Nguyen, Q. O. Lawal, A. Chortos, S. Rondeau-Gagne, Z. N. Bao, *Adv. Mater.* **2015**, *27*, 6954.
[38] R. A. Surmenev, T. Orlova, R. V. Chernozem, A. A. Ivanova, A. Bartasyte, S. Mathur, M. A. Surmeneva, *Nano Energy* **2019**, *62*, 475.
[39] J. Glaum, M. Hoffman, *J. Am. Ceram. Soc.* **2014**, *97*, 665.
[40] W. Liu, X. Ren, *Phys. Rev. Lett.* **2009**, *103*, 257602.
[41] L. Dong, A. B. Closson, C. Jin, Y. Nie, A. Cabe, D. Escobedo, S. Huang, I. Trase, Z. Xu, Z. Chen, M. D. Feldman, J. X. J. Zhang, *Adv. Healthcare Mater.* **2020**, *9*, 2000053.
[42] W. Li, N. Wu, J. Zhong, Q. Zhong, S. Zhao, B. Wang, X. Cheng, S. Li, K. Liu, B. Hu, J. Zhou, *Adv. Funct. Mater.* **2016**, *26*, 1964.
[43] X. Mo, H. Zhou, W. Li, Z. Xu, J. Duan, L. Huang, B. Hu, J. Zhou, *Nano Energy* **2019**, *65*, 104033.
[44] N. Wu, X. Cheng, Q. Zhong, J. Zhong, W. Li, B. Wang, B. Hu, J. Zhou, *Adv. Funct. Mater.* **2015**, *25*, 4788.
[45] Z. Xu, X. Wan, X. Mo, S. Lin, S. Chen, J. Chen, Y. Pan, H. Zhang, H. Jin, J. Duan, L. Huang, L.-B. Huang, J. Xie, F. Yi, B. Hu, J. Zhou, *Nano Energy* **2021**, *89*, 106450.
[46] X. Wan, P. Chen, Z. Xu, X. Mo, H. Jin, W. Yang, S. Wang, J. Duan, B. Hu, Z. Luo, L. Huang, J. Zhou, *Adv. Funct. Mater.* **2022**, *32*, 2200589.
[47] J. Zhong, Y. Ma, Y. Song, Q. Zhong, Y. Chu, I. Karakurt, D. B. Bogy, L. Lin, *ACS Nano* **2019**, *13*, 7107.
[48] S. Gong, B. Zhang, J. Zhang, Z. L. Wang, K. Ren, *Adv. Funct. Mater.* **2020**, *30*, 1908724.
[49] Z. Xia, R. Gerhard-Multhaupt, W. Künstler, A. Wedel, R. Danz, *J. Phys. D: Appl. Phys.* **1999**, *32*, L83.
[50] X. Zhang, J. Hillenbrand, G. M. Sessler, *Appl. Phys. A* **2006**, *84*, 139.
[51] B. Wang, C. Liu, Y. Xiao, J. Zhong, W. Li, Y. Cheng, B. Hu, L. Huang, J. Zhou, *Nano Energy* **2017**, *32*, 42.
[52] J. Hillenbrand, G. M. Sessler, *IEEE Trans. Dielectr. Electr. Insul.* **2004**, *11*, 72.
[53] C. L. Zhang, L. L. Zhou, P. Cheng, X. Yin, D. Liu, X. Y. Li, H. Y. Guo, Z. L. Wang, J. Wang, *Appl. Mater. Today* **2020**, *18*, 100496.
[54] S. M. Niu, S. H. Wang, L. Lin, Y. Liu, Y. S. Zhou, Y. F. Hu, Z. L. Wang, *Energy Environ. Sci.* **2013**, *6*, 3576.
[55] M. R. Angerame, D. C. Holst, J. M. Jennings, R. D. Komistek, D. A. Dennis, *J. Arthroplasty* **2019**, *34*, 2502.
[56] S. Yamauchi, K. Ishibashi, E. Sasaki, S. Sasaki, Y. Kimura, Y. Ishibashi, *J. Orthop. Surg. Res.* **2021**, *16*, 526.